Super-Resolution Hyperspectral Reconstruction with Majorization-Minimization Algorithm and Low-Rank Approximation

Ralph Abi Rizk, François Orieux, Alain Abergel

Super-Resolution Hyperspectral Reconstruction with Majorization-Minimization Algorithm and Low-Rank Approximation

Ralph Abi-Rizk, François Orieux and Alain Abergel

***Abstract*—Hyperspectral imaging (HSI) has become an invaluable imaging tool for many applications in astrophysics or Earth observation. Unfortunately, direct observation of hyperspectral images is impossible since the actual measurements are 2D and suffer from strong spatial and spectral degradations, especially in the infrared. We present in this work an original method for high-resolution hyperspectral image reconstruction from heterogeneous 2D measurements degraded by integral field spectroscopy (IFS) instrument. A fundamental part of this work is developing a forward model that accounts for the limitations of the IFS instrument, such as wavelength-dependent spatial and spectral blur, subsampling, and inhomogeneous sampling steps. The reconstruction method inverts the forward model using a deterministic regularization framework for edge-preserving. It fuses information from different observations and spectral bands for resolution enhancements. We rely on the Majorize-Minimize memory gradient (3MG) optimization algorithm to solve the inverse problem while considering a low-rank approximation for the unknown to handle the high-dimensionality of the problem.**

***Index Terms*—Inverse Problems – Super Resolution – Hyperspectral Imaging – Deconvolution – Spectral unmixing**

I. Introduction

HYPERSPECTRAL imaging (HSI) simultaneously collects high-resolution spectra at different spatial locations. It is wildly used for remote sensing applications in numerous domains such as in astrophysics [1], fluorescence microscopy [2], military [3], medical diagnosis [4], and others. HSI products are 3-dimensional (3D) images (i, j, l) where (i, j) are the two spatial dimensions and l the spectral dimension. Unfortunately, direct observations of hyperspectral (HS) images are not straightforward because 3D detectors do not exist. Instead, HS instruments, primarily relying on dispersive spectrometers, are designed to acquire measurements projected onto 2D detectors. In particular, HS instruments based on Integral Field Spectroscopy (IFS) [5] simultaneously observe the field of view (FOV) of the 3D input image through several thin slits in parallel. The dispersed wavelength from each slit is projected onto 2D detectors, spanning a spatial dimension along one axis and a spectral dimension along the other axis. Consequently, a reconstruction stage is required to estimate the 3D input image from the collected 2D measurements. Although having a high spectral resolution, the 2D measurements suffer from spatial and spectral limitations during the acquisition process, such as blurring, sampling, and noise. First, because of the diffraction [6], the optical response known as the Point Spread function (PSF) introduces a wavelength-dependent spatial blurring. Second, the response of the dispersing system introduces a spectral blurring, which is also wavelength-dependent [7]. Finally, the spatial sampling on the detector is often insufficient at all wavelengths. To enhance the spatial resolution lost at the detector, a "dithering" method is considered [8], [9], consisting of observing the same scene multiple times by slightly shifting the measuring instrument. The resulted multi-frame measurements lead to a Super Resolution (SR) problem [10].

Several multi-frame SR algorithms have been addressed to reconstruct a discrete 3D input image from a set of measurements degraded by the HS instrument. The state-of-art approach for multi-frame SR 3D reconstruction is based on the shift and addition (S&A) method [8], [11]. It merges the overall sampled and aliased measurements to provide a single reconstructed 3D image with an enhanced spatial resolution. Even though the S&A provides fast and non-iterative algorithms, it does not consider spatial and spectral blurring. Hence, it can be followed by a deblurring step, such as a Total Variation (TV) regularization [12], [13]. This technique is efficient for monochromatic image reconstruction. However, for HS image reconstruction, the deblurring step treats the spatial and spectral dimensions separately without considering the correlations between spectral bands.

Multi-frame SR reconstruction algorithms for HS images have also been treated as an inverse problem allowing a joint process of the spatial and spectral information from all the measurements. Such approaches rely on an explicit forward model that considers the limitations of the HS instrument and some additional priors about the 3D input image [14], [15]. Other tensor-based methods for HS reconstruction have been proposed in [16] for SR, deblurring and denoising. Most of these approaches assume a low-rank structure, where the input is represented with a small number of spectral components.

[14] developed a forward model that simulates optically blurred, sampled, and aliased HS multi-frame measurements. They proposed a SR reconstruction algorithm based on the projection onto convex sets (POCS) method [17] that relies on the forward model to restore the observed HS image,

R. Abi-Rizk and F. Orieux are at the Laboratoire des Signaux et Systèmes, Université Paris-Saclay, CNRS, CentraleSupélec, 3 rue Joliot-Curie, 91190 Gif-Sur-Yvette, France, e-mail: *name@l2s.centralesupelec.fr*

A. Abergel is at the Institut d'Astrophysique Spatiale, Université Paris-Saclay, CNRS, 91405 Orsay, France

This project is co-funded by CNES. This work was performed using HPC resources from the "Mésocentre" computing center of CentraleSupélec and École Normale Supérieure Paris-Saclay supported by CNRS and Région Île-de-France (http://mesocentre.centralesupelec.fr/)

approximated in the low-dimensional subspace. [15] handled the multi-frame SR reconstruction in the principal component analysis (PCA) domain. They used the first few principal components [18] to estimate motion and to reconstruct the 3D input image via the maximum a posteriori (MAP) [19]. However, the spatial blurring considered in these works is stationary, and the spatial and spectral fields of view are homogeneous.

Another solution for the spatial resolution enhancement is to perform a fusion of spatially sampled HS measurements with an auxiliary image of the same scene with high spatial resolution, if available, such as panchromatic (PAN) [20], or multispectral (MS) [1]. In particular, the HS-MS fusion has been excessively addressed in the inverse problem framework [1], [21], [22]. It relies on minimizing an objective function associated with two data fitting terms for HS and MS, respectively, and some priors about the 3D input image. [1] proposed an HS-MS fusion method while accounting for wavelength-dependent spatial blur. They provide fast algorithms in the Fourier domain while assuming a low-rank structure of the astronomical input image. However, the works proposed in [1], [14], [15] consider 3D measurements with uniform spatial and spectral sampling steps and without accounting for a wavelength-dependent spectral PSF.

We present in this work a complex forward model based on an IFS instrument dedicated to astronomical observations in the infrared spectral range. The input is a 3D spatio-spectral image with a high resolution, approximated in a low-rank subspace, and simulates a set of multi-frame measurements projected onto different 2D detectors of different characteristics. The proposed model allows different input observations from different IFS instruments and pointing. Moreover, it considers wavelength-dependent spatial and spectral blurring, as well as heterogeneous spatial and spectral sampling on the detectors. We then propose a reconstruction method that uses the forward model and relies on the regularized least square approaches with convex edge-preserving regularization [23]. To solve the inversion problem, we choose the iterative Majorize-Minimize Memory Gradient (3MG) optimization algorithm [24] tested on two synthetic 3D input images with different spatial and spectral distributions. The results show significant improvement of the spatial and spectral resolutions compared to the shift-and-add (S&A) algorithm [8], [11] followed by a spatial Total-Variation (TV) regularization for each wavelength [12], and the classic l_2 regularization [25].

The paper is organized as follows. The section II discusses the proposed methodology, first for the instrument model developed for the IFS instrument (Section II-A), and second for the forward model based on the linear mixing model (LMM) [26] (Section II-B). The SR multi-frame reconstruction algorithm is presented in Section III. In Section IV, we present the reconstruction results with the proposed algorithm and provide a comparison with other reconstruction algorithms. Finally, we provide a conclusion in Section V.

II. Forward Model for Heterogenous Hyperspectral Data Fusion

A. Observation Model

This section presents a new observation model of IFS instruments used for spectral data fusion. It considers a series of components that modify and degrade the observed 3D input image (HS image), resulting in a set of blurred, truncated, and aliased 2D multi-frame measurements.

The original discretized input image is denoted $\boldsymbol{x}[i,j,l]$, with two spatial dimensions $(i,j) \in [1,\dots,I] \times [1,\dots,J]$ denoting the pixel index, and one spectral dimension $l \in [1,\dots,L]$. It is supposed uniformly sampled with spatial steps (T_i, T_j), and spectral step T_l.

1) Spatial Filtering: Because of the diffraction phenomenon [6], the observed 3D input is spatially blurred by the response of the optical system, also known as the point spread function (PSF). The PSF, denoted $\boldsymbol{h}$, is spectrally non-invariant, with an increasing blur as the wavelength increases. We suppose that the monochromatic PSF is known from simulations [27], calibration, or previous data processing steps. The PSF is also assumed to be spatially stationary at all wavelengths. Thus, the spatial filtering is carried out by a 2D spatial convolution between the 3D input image and a discrete wavelength-dependent PSF, sampled with the same sampling step of the input, (T_i, T_j), writing

$$\boldsymbol{x}_{\text{opt}} = \boldsymbol{x}[i,j,l] \underset{i,j}{*} \boldsymbol{h}[i,j,l]. \tag{1}$$

We will see in the next section that the model includes spatially truncated observation since the field of view of the IFS instrument is smaller than that of the 3D input image. Consequently, the spatial convolution is calculated using the discrete spatial Fourier transform for fast computation [28] without introducing periodic patterns to the blurred image.

2) Spatio-Spectral Field of View: We consider here a spectral data fusion problem where $\boldsymbol{x}_{\text{opt}}$ is observed with various spatial and spectral fields of view grouped in distinct spectral channels $c \in [1,\dots,C]$. Each channel can possess a different FOV, spectral range, and sampling step size. In addition, the IFS instrument observes the FOV of each channel simultaneously through several slits in parallel. The number and size of the slits depend on the channel c. The spectral selection into channels and the spatial selection into slits result from a multiplication between $\boldsymbol{x}_{\text{opt}}$ and the channel windows $\boldsymbol{w}_c$ that writes

$$\boldsymbol{w}_c[i,j,l] \neq 0, \quad \forall (i,j,l) \in (\mathcal{I}_c, \mathcal{J}_c, \mathcal{L}_c), \tag{2}$$

with $(\mathcal{I}_c, \mathcal{J}_c, \mathcal{L}_c)$ a rectangular subset of $[1,\dots,I] \times [1,\dots,J] \times [1,\dots,L]$, and 0 otherwise. This hypothesis implies that all window sizes $(\Delta_{i,c}, \Delta_{j,c})$ are multiples of the step sizes of the 3D input image $\boldsymbol{x}$: $(\Delta_{i,c}, \Delta_{j,c}) = (n_c T_i, m_c T_j)$, with $(n_c, m_c) \in \mathbb{N}^2$. This is an approximation, minored if the step sizes are small.

In addition, the instrument enables different pointing (spatial shifts or dithering), indexed by p, that can be shared between channels. We also consider that the pointing positions $(\Delta_{i,p}, \Delta_{j,p})$ are multiples of the sampling steps of $\boldsymbol{x}$: $(\Delta_{i,p}, \Delta_{j,p}) = (i_p T_i, j_p T_j)$, with $(i_p, j_p) \in \mathbb{N}^2$.

Finally, the spatio-spectral field of view for a particular pointing writes

$$\boldsymbol{x}_{c,p}[i,j,l] = \boldsymbol{x}_{\text{opt}}[i,j,l] \times \boldsymbol{w}_c[i-i_p, j-j_p, l]. \quad (3)$$

3) Spectral Blurring: The spatio-spectral cubes $\boldsymbol{x}_{c,p}[i,j,l]$ are projected onto 2D detectors, through diffraction gratings for instance. For a monochromatic punctual source at the wavelength $\lambda = lT_l$ from the channel c and the pointing p, we consider the usual spectral response for grating spectrometers writing [29]

$$h_{c,j,p}(l',l) \propto \text{sinc}^2\left(\pi W\left(\frac{l'T_{l'} - q_{j,p}}{lT_l} - 1\right)\right). \quad (4)$$

Here $\lambda' = l'T_{l'}$ is the spatial position on the detector (in wavelength units) with a sampling step $T_{l'}$, and $q_{j,p} \in [-\Delta_{j,c}/2, \Delta_{j,c}/2]$ is the *relative* spatial position of the input source determined by the spatial position j and the pointing p. This spectral response is independent of the other spatial position indexed by i. Moreover, as pointed by Eq. (5) below, the proposed model is not limited to the spectral PSF detailed in Eq. (4). Other models or responses inferred from calibrations can also be considered.

Several particularities of the spectral response, or more generally of the dispersion system, are inferred from Eq. (4). First, as illustrated in Fig. 1, the spatial position on the detector $\lambda' = l'T_{l'}$ of the spectral response depends on the wavelength input $\lambda = lT_l$. Second, the spectral response is *not stationary* and becomes broader with the increase of the wavelength. Finally, the relative spatial position $q_{j,p}$ alters the spatial position of the spectral response on the detector by shifting its maximum position.

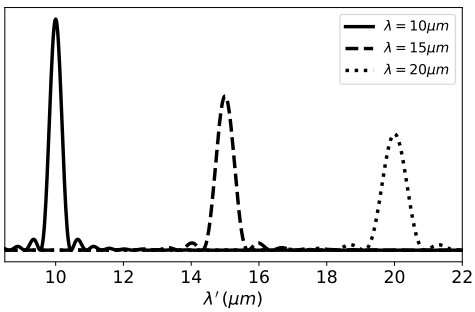

Fig. 1. Grating outputs (from Eq. (4)) for three monochromatic point sources at different wavelengths ($\lambda = lT_l$). The position on the detector ($\lambda' = l'T_{l'}$) depends on λ, while the width increases linearly with the wavelength.

Eq. (4) also depends on the parameter W. It defines the width of the spectral response, which controls the spectral resolution. Assuming that the instrument is calibrated with a known spectral resolution $R = \lambda/\Delta\lambda$, with $\Delta\lambda$ the full width at half maximum (FWHM), basic calculus leads to $W \approx 2.8R/\pi$. Finally, the grating is a non-stationary linear system.

After discretization of the response, all individual sources $\boldsymbol{x}_{c,p}[i,j,l]$ contribute on the detector resulting in an output $\boldsymbol{g}_{c,p}$ of the dispersing system that writes

$$\boldsymbol{g}_{c,p}[i,j,l'] = \sum_{l \in \mathcal{L}_c} \boldsymbol{x}_{c,p}[i,j,l] \boldsymbol{h}_{c,j,p}[l',l], \quad (5)$$

with $l' \in \mathcal{L}'_c$ the wavelength index sampled on the detector and $\boldsymbol{h}_{c,j,p}[l',l]$ obtained from Eq. 4. The model in Eq. (5) is not a convolution since the spectral response is not stationary. Consequently, homogeneous spectral sampling is not required and can vary across the channels c. The spectral resolution of the output is fixed by the spectral response and depends on the sampled wavelength l'.

4) Detector Integration: The 3D spatially and spectrally blurred cube $\boldsymbol{g}_{c,p}[i,j,l']$ depends on the spatial index j whereas detectors are 2D. Since the system is linear, all the contributions of sources within the spatial window $\mathcal{J}_{c,p}$, determined by the channel c and pointing p, are summed on the detector. Consequently, without dithering and super-resolution, the width of the window $\boldsymbol{w}_c$ along the j-axis of the measurements determines the spatial resolution along this axis.

Moreover, the spatial sampling step T_i along the i-axis of the object $\boldsymbol{g}$ is different and smaller than the sampling step of the detector. Therefore, for all pointing p, we consider that the spatial sampling step $T_{i'}$ of the detectors for each channel c is a multiple $d_c \in \mathbb{N}$ of T_i with $T_{i'} = d_c T_i$, as in the classical image Super-Resolution [10]. Consequently, the 2D measurement $\boldsymbol{y}_{c,p}$ for channel c and pointing p writes

$$\boldsymbol{y}_{c,p}[i',l'] = \sum_{i=i'd_c}^{(i'+1)d_c-1} \sum_{j \in \mathcal{J}_{c,p}} \boldsymbol{g}_{c,p}[i,j,l'] \quad (6)$$

where i' and l' are the spatial and spectral indexes on the 2D detector, respectively. In practice, the summation along the i-axis is computed as a convolution between $\boldsymbol{g}$ and a square impulse response of size d_c, followed by subsampling every d_c elements.

To conclude, we have developed a non-stationary but linear forward model involving relatively complex components that writes

$$\boldsymbol{y}_{c,p}[i',l'] = \sum_{i,j} \sum_{l \in \mathcal{L}_c} \left(\boldsymbol{x}[i,j,l] \underset{i,j}{*} \boldsymbol{h}[i,j,l]\right) \boldsymbol{w}_c[i-i_p, j-j_p, l] \times \boldsymbol{h}_{c,j,p}[l',l], \quad (7)$$

and accounts for several effects:

- 2D spatial convolutions with spectrally varying PSF described in Eq. (1) to model the optics,
- spatio-spectral windowing defined in Eq. (3) that models different spatial pointing, and different spatio-spectral selections,
- spectral blurring with a non-stationary response described in Eq. (5),
- and spatial and spectral sampling with specific steps for each detector which are larger than the sampling steps of the 3D input, described in Eq. (6).

The next section presents the combination of this observation model with a subspace representation of the 3D input image.

B. LMM forward model

1) Linear Mixing Model: Without additional information, the reconstruction of $\boldsymbol{x}$ corresponds to the estimation of

each voxel $\boldsymbol{x}[i,j,l]$ from the set of measurements $\{\boldsymbol{y}_{c,p}\}$ for all channels c and all pointing p. However, the spectral information contained in the 3D input images can be complex, with spectral rays, non-monochromatic spectral features, and continuum. Moreover, this spectral information is generally highly correlated between spatial pixels over the whole measured spectral range. Therefore, dimension reduction methods such as Principal Component Analysis (PCA) [18] or Non-negative Matrix Factorization (NMF) [30] can be very efficient on 3D images with a high spectral resolution, such as HS images.

Here we propose to write the unknown 3D image $\boldsymbol{x}$ using a Linear Mixing Model writing

$$\boldsymbol{x}[i,j,l] = \sum_{m=1}^{M} \boldsymbol{a}_m[i,j] \times \boldsymbol{s}_m[l] \tag{8}$$

where the spectral distribution at each spatial position (i,j) is a linear combination of M spectral components $\boldsymbol{s}_m$, known *a priori* or learned from the measurements, and unknown proportions $\boldsymbol{a}_m$. For our purposes, this is a subspace approximation as the number of spectral components M is much lower than the number of spectral bands L, as observed with dimension reduction methods [1]. For earth observation with segmentation problems, the spectral components $\boldsymbol{s}_m$ are pure spectra called end-members, and the $\boldsymbol{a}_m$ coefficients are called abundances [26]. In that case, additional constraints are usually imposed on $\boldsymbol{a}_m$ such as the non-negativity and sum-to-one constraints. This is not our case since we are only interested in the subspace approximation to reconstruct the original unknown 3D image $\boldsymbol{x}$, and not in the physical meaning of the spectral components $\boldsymbol{s}_m$.

The linear mixing model preserves the spatial and spectral distributions of the 3D input image and has many advantages:

- The subspace approximation significantly reduces the number of unknowns that we want to estimate.
- As a consequence it is expected to increase the Signal-to-Noise (SNR) ratio on the reconstructed object.
- The reconstruction problem is limited to the estimation of the mixing coefficients $\boldsymbol{a}_m$, which requires only a spatial regularization to enhance the spatial resolution of the estimated 3D image.
- As the reconstruction of $\boldsymbol{x}$ is a linear combination of the estimated $\boldsymbol{a}_m$ and the known $\boldsymbol{s}_m$, the final spectral resolution of the reconstructed object is the spectral resolution of the spectral components $\mathbf{s}_m$.
- The spectral information is fully given regardless of the channel characteristics, while the spatio-spectral reconstruction of $\boldsymbol{x}$ directly from the measurements, without considering the mixing model, cannot exploit the complete spectral information at all spatial positions since the observation model (see Sec. II-A2) considers different FOV depending on the channel.
- The estimated unknowns $\boldsymbol{a}_m$ depends solely on the spatial information. Hence, all spectral related terms (that depends on l and l') can be precomputed.

[1]If $M \gg L$, the reconstruction problem with an overcomplete dictionary is considered, leading to variable selection methods, often done with sparsity, outside the scope of this work.

2) Final Forward Model: By combining the linear mixing model in Eq. (8) with the observation model in Eq. (7) we obtain

$$\boldsymbol{y}_{c,p}[i',l'] = \sum_{i,j} \sum_{l\in\mathcal{L}_c} \left(\left[\sum_{m=1}^{M} \boldsymbol{a}_m[i,j]\boldsymbol{s}_m[l] \right] \underset{i,j}{*} \boldsymbol{h}[i,j,l] \right) \boldsymbol{w}_c[i-i_p, j-j_p, l] \times \boldsymbol{h}_{c,j,p}[l',l]. \tag{9}$$

The above equation can be directly used to compute the forward output. However, since we want to estimate the mixing coefficients $\boldsymbol{a}_m$ and not the full 3D input image $\boldsymbol{x}$, the known spectral components $\boldsymbol{s}_m$ can be included in the observation model. Consequently, a new spectral dependent forward model is formulated that directly links the mixing coefficients to the measurements. For that purpose, all spectral operations related to l and l' can be combined and precomputed.

First a spatial PSF cube *that depends on* m is computed for each spectral component with $\boldsymbol{h}_m[i,j,l] = \boldsymbol{s}_m[l]\boldsymbol{h}[i,j,l]$. The model then writes

$$\boldsymbol{y}_{c,p}[i',l'] = \sum_{i,j} \sum_{l\in\mathcal{L}_c} \left(\sum_{m=1}^{M} \boldsymbol{a}_m[i,j] \underset{i,j}{*} \boldsymbol{h}_m[i,j,l] \right) \boldsymbol{w}_c[i-i_p, j-j_p, l] \times \boldsymbol{h}_{c,j,p}[l',l]. \tag{10}$$

Second, the spectral blurring of $\boldsymbol{s}_m$ introduced by the spectral response $\boldsymbol{h}_{c,j,p}$ in Eq. (4) can be precomputed with

$$\boldsymbol{h}_{m,c,j,p}[i,j,l'] = \sum_{l\in\mathcal{L}_c} \boldsymbol{s}_m[l]\boldsymbol{h}[i,j,l]\boldsymbol{w}_c[l]\boldsymbol{h}_{c,j,p}[l',l] \tag{11}$$

where $\boldsymbol{h}_{m,c,j,p}[i,j,l']$ is a spatio-spectral PSF cube that depends on the spectral template number m, the spectral window $\mathcal{L}_c$, and relative position j within the spatial window $\mathcal{J}_{c,p}$ (as described by Eq. (4)). Finally, the forward model writes

$$\boldsymbol{y}_{c,p}[i',l'] = \sum_{i} \sum_{j\in\mathcal{J}_{c,p}} \boldsymbol{w}_c[i-i_p, j-j_p] \left(\sum_{m=1}^{M} \boldsymbol{a}_m[i,j] \underset{i,j}{*} \boldsymbol{h}_{m,c,j,p}[i,j,l'] \right). \tag{12}$$

Compared to Eq. (9), the final forward model is relatively simplified with the following steps:

- First, the 2D mixing coefficients $\boldsymbol{a}_m$ are convoluted by a collection of 2D+λ PSF $\boldsymbol{h}_{m,c,j,p}$ that depends on the spectral component number m, the channel c, and the relative spatial position within the channel (j,p).
- After summation on m, the cube is spatially windowed for each pointing p.
- Then, the high-resolution window is spatially detector integrated (subsampled), resulting in 2D measurements $\boldsymbol{y}_{c,p}$ with a low spatial resolution.

3) Matrix Formulation: The model in Eq. (12) is linear and represents the overall multi-frame 2D measurements $\boldsymbol{y}_{c,p}$ in terms of the unknown mixing coefficients $\boldsymbol{a}$

$$\boldsymbol{y}_{c,p} = \boldsymbol{H}_{c,p}\boldsymbol{a} = \boldsymbol{\Sigma}_{i,j}\boldsymbol{W}_c\boldsymbol{\Sigma}_m\boldsymbol{C}_{m,c,j,p}\boldsymbol{a} \tag{13}$$

where $\boldsymbol{C}$ is a convolution operator, $\boldsymbol{\Sigma}_m$ a summation on the spectral template number m, $\boldsymbol{W}_c$ a windowing or raw selection and $\boldsymbol{\Sigma}_{i,j}$ a sum on i, j to model detector integration.

Consequently, the adjoint operator writes

$$\boldsymbol{e}_{c,p} = \boldsymbol{H}_{c,p}^T \boldsymbol{y}_{c,p} = \boldsymbol{C}_{m,c,j,p}^T \boldsymbol{\Sigma}_m^T \boldsymbol{W}_c^T \boldsymbol{\Sigma}_{i,j}^T \boldsymbol{y}_{c,p} \tag{14}$$

where $\boldsymbol{\Sigma}^T$ is a duplication operator, $\boldsymbol{W}_c^T$ a zero filling operator and $\boldsymbol{C}_{m,c,j,p}^T$ a convolution with flipped response.

The overall measurements writes

$$\boldsymbol{y} = \boldsymbol{H}\boldsymbol{a} = [\boldsymbol{H}_{0,0}^T, \ldots, \boldsymbol{H}_{C,P}^T]^T \boldsymbol{a} \tag{15}$$

and the full-adjoint operator writes

$$\boldsymbol{e} = \sum_{c,p} \boldsymbol{H}_{c,p}^T \boldsymbol{y}_{c,p} = \boldsymbol{H}^T \boldsymbol{y} \tag{16}$$

which is the sum of all retro-propagated measurements.

The next section describes the proposed reconstruction formalized as an inverse problem approach with efficient Quadratic Majorize-Minimize algorithm [24], [31].

III. Inverse problem

Our new forward model combines multiple observations with a full complex linear model $\boldsymbol{y} = \boldsymbol{H}\boldsymbol{a}$. The operator $\boldsymbol{H}$ takes into account (1) spectral-dependent spatial blurring, (2) multiple channel observations with different fields of view, (3) spectral blurring, and (4) heterogeneous spatial and spectral samplings. Therefore, the mixing coefficient $\boldsymbol{a}$ reconstruction is an ill-posed inverse problem that includes data fusion, deconvolution, and multi-frame super-resolution steps.

A. Proposed reconstruction

We propose a new multi-frame SR algorithm that relies on the complete forward model in Eq. (12), with a reconstruction solution defined as the minimizer of an objective function combining a data fidelity term and a regularization term $R(a)$ expressed as

$$\hat{\boldsymbol{a}} = \arg\min_{\boldsymbol{a}} \left(\|\boldsymbol{y} - \boldsymbol{H}\boldsymbol{a}\|_{\boldsymbol{\Sigma}^{-1}}^2 + R(\boldsymbol{a}) \right) \tag{17}$$

where $\boldsymbol{\Sigma}$ is the noise covariance matrix. We suppose here that the noise is Gaussian but not necessarily identically distributed or independent. However, the application of the inverse covariance matrix must be feasible. This model can approximate in some way Poisson noise with high photon count with independent non-identically distributed Gaussian noise. In that case, $\boldsymbol{\Sigma}^{-1}$ is diagonal with values that should be derived from measurements. Many regularization methods and algorithms have been proposed in the literature. For instance, l_2 regularization [25] is the seminal approach with fast algorithms but fails to preserve the high gradient values of the solution. The Total Variation (TV) regularization [12] or dictionary-based approaches with sparsity constraints [32] has been broadly used but can introduce cartoon-like effects and provide relatively slow algorithms. More recently, prior learning from data with machine learning approaches [33] has been widely explored but requires many measurements to be competitive.

In this work, the major degradation effects of the forward model are the spectral-dependent spatial and spectral blurring. However, by choosing a linear mixing model with known spectral components $\boldsymbol{s}$, our reconstruction algorithm does not require spectral regularization. On the other hand, the spatial blurring is significant, especially at long wavelengths. Therefore, we propose a convex spatial regularization to preserve strong spatial gradient in the image. The objective function, denoted $J(\boldsymbol{a})$, writes

$$J(\boldsymbol{a}) = \|\boldsymbol{y} - \boldsymbol{H}\boldsymbol{a}\|_{\boldsymbol{\Sigma}^{-1}}^2 + \mu \sum_{c \in \mathcal{C}} \phi(\boldsymbol{v}_c^T \boldsymbol{a}) \tag{18}$$

where $\boldsymbol{v}_c$ are first-order differences in the two spatial dimensions, $c \in \mathcal{C}$ a clique index that is a linear combination of pixels, μ is the spatial regularization parameter, and ϕ is a strictly differentiable convex loss like the Huber loss, allowing the use of fast optimization algorithms like [24], often faster than those based on non-differentiable loss [34]. Moreover, these algorithms are not restricted to convex loss.

B. Quadratic Majorization Minimization

The objective function $J(\boldsymbol{a})$ is an instance of the more general criterion [23], [35] with:

$$J(\boldsymbol{a}) = \sum_q \mu_q \Psi_q(\boldsymbol{\mathcal{V}}_q \boldsymbol{a}_q - \boldsymbol{\omega}_q) \tag{19}$$

where $\boldsymbol{a}$ is the unknown, $\boldsymbol{\mathcal{V}}_q$ is a linear operator, $\boldsymbol{\omega}_q$ is a data fixed vector, μ_q are scalar hyper-parameters, and $\Psi_q(\boldsymbol{u}) = \sum_c \phi_q(u_c)$.

In addition, we suppose the following assumptions for the scalar function ϕ_q [24]:

1) $\mathcal{C}^1$, even, coercive,
2) $\phi_q(\sqrt{\cdot})$ is concave on $\mathbb{R}^+$,
3) and $0 < \dot{\phi}_q(u)/u < +\infty$, $\forall u \in \mathbb{R}$.

This objective function structure is chosen to allow efficient algorithms that use majorization with quadratic surrogate functions Q which write [36]

$$Q\left(\boldsymbol{a}, \boldsymbol{a}^k\right) = J\left(\boldsymbol{a}^k\right) + \nabla J\left(\boldsymbol{a}^k\right)^T \left(\boldsymbol{a} - \boldsymbol{a}^k\right) + \frac{1}{2}\left(\boldsymbol{a} - \boldsymbol{a}^k\right) \boldsymbol{A}^{(k)} \left(\boldsymbol{a} - \boldsymbol{a}^k\right) \tag{20}$$

where

$$\boldsymbol{A}^{(k)} = \sum_q \mu_q \boldsymbol{\mathcal{V}}_q^T \operatorname{diag}(\boldsymbol{b}_q^k) \boldsymbol{\mathcal{V}}_q$$

and

$$\boldsymbol{b}_q^k = \frac{\dot{\phi}(\boldsymbol{\mathcal{V}}_q \boldsymbol{x}^k - \boldsymbol{\omega}_q)}{\boldsymbol{\mathcal{V}}_q \boldsymbol{x}^k - \boldsymbol{\omega}_q}. \tag{21}$$

Lemma 3.1: [36] Let J be the objective function defined in Eq. (19) and $\boldsymbol{a}^k \in \mathbb{R}^N$. If the assumption holds, then the quadratic surrogate function Q in (20) is a tangent majorant for J at $\boldsymbol{a}^k$, for all $\boldsymbol{a} \in \mathbb{R}^N$,

$$\begin{cases} Q(\boldsymbol{a}, \boldsymbol{a}^k) \geq J(\boldsymbol{a}), \\ Q(\boldsymbol{a}^k, \boldsymbol{a}^k) = J(\boldsymbol{a}^k). \end{cases} \tag{22}$$

The proposed criterion in Eq. (18) is an instance of Eq. (19) with $q = \{1, 2\}$, $\mu_1 = 1$, $\Psi_1(\cdot) = \|\cdot\|_{\boldsymbol{\Sigma}^{-1}}^2$, $\boldsymbol{\omega}_1 = \boldsymbol{y}$, $\boldsymbol{\mathcal{V}}_1 = \boldsymbol{H}$,

$\boldsymbol{\mathcal{V}}_2 = \boldsymbol{V} = [\boldsymbol{v}_1, \ldots, \boldsymbol{v}_\mathcal{C}]^T$. In case of quadratic loss like Ψ_1, the curvature matrix $\boldsymbol{A}$ does not change, includes $\boldsymbol{\Sigma}$, and $\boldsymbol{b}$ variables equal 1. In previous work [37], we considered the half quadratic (HQ) strategy proposed by Geman and Reynolds (GR) [35] that use quadratic surrogate function on all space $\mathbb{R}^N$. However, in our case, the computational cost remains important since our forward model is complex and works on high-dimensional input object and data. We therefore choose to adopt recent and efficient algorithms based on this Majorize-Minimize but for the step strategy applied on subspace optimization [24], [38].

C. Subspace Optimization With Majorize-Minimize Step

Since the criterion in Eq. (18) is differentiable (and convex if ϕ is convex), the optimization can be done with Non-Linear Conjugate Gradient [39], or more efficiently with subspace optimization methods that are known to be the most efficient for this kind of criterion [40]. In the latter case, the iterative algorithm writes

$$\boldsymbol{a}^{(k+1)} = \boldsymbol{a}^{(k)} + \alpha^{(k)}\boldsymbol{g}^{(k)} + \sum_{z=1}^{Z} \beta^{(k,z)}\boldsymbol{d}^{(k-z)} \tag{23}$$

where $\boldsymbol{g}^{(k)} = \nabla J(\boldsymbol{a}^{(k)})$ is the gradient of $J(\boldsymbol{a}^{(k)})$ at the iteration k, $\boldsymbol{d}^{(k-z)}$ are the previous descent directions, and $\alpha^{(k)}$ and $\beta^{(k,z)}$ are scalars.

We particularly rely on the Majorize-Minimize Memory Gradient (3MG) algorithm [24] that exploits the structure of the criterion in Eq (18) to compute both the steps α and the conjugacy parameter $\beta^{(z)}$ via the Majorize-Minimize strategy, like in Sec. III-B. Therefore, Eq. (23) can be rewritten as

$$\boldsymbol{a}^{(k+1)} = \boldsymbol{a}^{(k)} + \boldsymbol{D}^{(k)}\boldsymbol{\alpha}^{(k)} \tag{24}$$

where $\boldsymbol{D}^{(k)}$ is the subspace of dimension Z and $\boldsymbol{\alpha}^{(k)}$ a vector of steps of size Z. Contrary to the traditional line search strategy, finding the steps can be done with the Quadratic Majorize-Minimize strategy in this subspace leading to an explicit formula of $\boldsymbol{\alpha}^{(k)}$ with

$$\boldsymbol{\alpha}^{(k)} = -\boldsymbol{U}^{(k)^{-1}} \nabla\, J^{(k)}\Big|_{\boldsymbol{\alpha}} \left(\boldsymbol{a}^{(k)} + \boldsymbol{D}^{(k)}\boldsymbol{\alpha}^{(k)}\right) \tag{25}$$

with $\boldsymbol{U}^{(k)} = \boldsymbol{D}^{(k)^t}\boldsymbol{A}^{(k)}\boldsymbol{D}^{(k)}$ a $Z \times Z$ matrix. Eq. (25) corresponds to the explicit solution of a quadratic loss that majorizes the original criterion (Eq. (18)) in the subspace generated by $\boldsymbol{D}^{(k)}$. In our experiments, we choose $Z = 2$, that is a subspace of size 2 where search direction consists of the gradient and the previous search $\boldsymbol{D}^{(k-1)}\boldsymbol{\alpha}^{(k-1)}$. Note that this strategy leads to an efficient algorithm that mainly needs the computation of the gradient (therefore, one application of $\boldsymbol{H}$ and $\boldsymbol{H}^T$ per iteration, the heaviest part of the whole algorithm) and the inversion of a $Z \times Z$ matrix. Moreover, this algorithm has guaranteed convergence, and we refer to [24] for more details.

IV. Experimental Results

This section tests the proposed reconstruction algorithm on two synthetic 3D spatio-spectral images with various spatial and spectral distributions. The developed forward model is general but primarily adapted for the Medium-Resolution Spectrometer of the Mid-Infrared Instrument (MIRI/MRS) onboard the James Webb Space Telescope (JWST), measuring in the infrared spectral range, from 4.9 and 28.3 μm [41].

We compare the proposed algorithm to the state-of-art, which is the shift-and-add (*S&A*) reconstruction algorithm [42], [8] followed by a TV regularization. First, the *S&A* method shifts the overall measurements $\boldsymbol{y}_{c,p}[i', l']$ from all channels c and pointing p in order to align them (after a pre-processing step of the raw data). The results are then co-added, resulting in a reconstructed hyperspectral image with enhanced spatial resolution. This method corresponds to minimizing a least square criterion with

$$J(\boldsymbol{x}) = \|\boldsymbol{y} - \boldsymbol{S}\boldsymbol{x}\|^2 \tag{26}$$

with $\boldsymbol{y}^t = [\boldsymbol{y}_{0,0}^T, \ldots, \boldsymbol{y}_{C,P}^T]$ and $\boldsymbol{S}^t = [\boldsymbol{S}_{0,0}^T, \ldots, \boldsymbol{S}_{C,P}^T]$. $\boldsymbol{S}_{c,p}$ is a sampling and summation matrix that models detector sampling but neglect blurring. The solution then writes

$$\boldsymbol{x}_{S\&A} = (\boldsymbol{S}^T\boldsymbol{S})^{-1} \sum_{c,p} \boldsymbol{S}_{c,p}^T \boldsymbol{y}_{c,p} \tag{27}$$

where $\boldsymbol{S}_{c,p}^T$ is an upsampling matrix, and $(\boldsymbol{S}^T\boldsymbol{S})^{-1}$ is a diagonal normalization matrix that counts the number of times a pixel is measured.

Since the *S&A* algorithm does not account for the blurring, it is usually followed by a deconvolution step. In this work, we chose a TV regularization for spatial deconvolution at each wavelength l', implemented with the primal-dual Chambolle-Pock algorithm [43] writing

$$\hat{\boldsymbol{x}}_{S\&A}^{l'} = \arg\min_{\boldsymbol{x}} \left(\|\boldsymbol{y} - \boldsymbol{H}^{l'}\boldsymbol{x}^{l'}\|_2^2 + \mu |\nabla \boldsymbol{x}^{l'}|_1 \right) \tag{28}$$

where $\boldsymbol{H}^{l'}$ is a spatial convolution operator for the wavelength l' and $\nabla \boldsymbol{x}^{l'}$ is the first-order difference of the spatial image for the same wavelength. This method does not allow data fusion since the spatial information is treated separately for every wavelength.

Finally, to highlight the importance of the edge-preserving regularization choice (see section III-A), especially for 3D input images with sharp edges, our algorithm is also compared to the classic l_2 regularization [25]

$$\hat{\boldsymbol{a}}_{\mathrm{q}} = \arg\min_{\boldsymbol{a}} \left(\|\boldsymbol{y} - \boldsymbol{H}\boldsymbol{a}\|_{\boldsymbol{\Sigma}^{-1}}^2 + \mu \|\boldsymbol{V}\boldsymbol{a}\|^2 \right) \tag{29}$$

solved via the conjugate-gradient optimization algorithm [44].

A. Setup of the experiment

We denote Obj_1 the first 3D input image, representing a synthetic object for which the results are easily interpretable. Obj_1 lives in a low-dimensional space, and expressed as a linear combination of $M = 3$ known spectral components $\mathbf{s}_m$ computed from astrophysical measurements [45], weighted by mixing coefficients $\boldsymbol{a}_m$ with sharp edges (see figure 3).

The second 3D input image, Obj_2, represents an astrophysical simulation of the photodissociation region located in the "*Orion bar*" also with known abundances and spectral components both available from [46]. It is made of $M = 4$

complex spectral distributions, containing sharp spectral lines and continuum emission, each weighted by their corresponding mixing coefficient a_m, which presents structures in a wide range of spatial scales (see figure 4).

Both input images are represented on a 3D Cartesian grid with $I \times J = 120 \times 120$ pixels with a spatial sampling step of $T_i = T_j = 0.1$ arcseconds. The spectral dimension for both input images measures the infrared spectral range from $4.85\,\mu$m to $28.5\,\mu$m. Obj_1 counts $L = 3500$ wavelengths uniformly sampled with a step $T_l = 6.7\,10^{-3}\,\mu$m, whereas, Obj_2 counts $L = 3551$ wavelengths non-uniformly sampled with a step T_l varying from $2.4\,10^{-3}$ to $1.4\,10^{-2}\,\mu$m.

The spectral dimension is divided by the HS instrument into four distinct spectral channels, with different spectral ranges, FOV, slit width, and numbers (see table I). The optical component of the HS instrument is limited by the diffraction [6] with a PSF assumed known. The analytic form of the PSF for a monochromatic wavelength λ can be theoretically obtained from the Fourier transform of the aperture function of the telescope. The PSF width depends on the wavelength, and its FWHM is $\simeq \lambda/D$ (radians), with D referring to the diameter of the telescope aperture. However, for the JWST, there is no exact analytical description of the aperture function. Thus, the PSF is numerically computed using the WebbPSF [27] package, developed by the Space Telescope Science Institute (STScI). Fig. 2 shows three monochromatic PSF at 5, 15, and $25\,\mu$m in logarithmic scales. It highlights the importance of considering a wavelength-dependent PSF in our model, especially since the FWHM of the PSF increases by a factor of 5 between the shortest and longest wavelength.

To allow multi-frame measurements, the forward model considers multiple observations of the same 3D input image, with a dithering pattern of 8 pointing directions. For a particular pointing, the light inside each spatio-spectral selection $\boldsymbol{x}_c$ is dispersed and projected onto 2D detectors with different spectral resolution R, and different spatial and spectral step sizes depending on the channel. The spatial step size of the measurements $T_{i'}$ is fixed by the spatial sampling of the detector. Given the large size of the MRS detectors, we consider in this work that the spectral step size of the measurements is $T_{l'} = 4 \times T_{l'}^{\text{MRS}}$ and the spectral resolution is $R = R^{\text{MRS}}/4$, in order to reduce the computational cost of the problem, where $T_{l'}^{\text{MRS}}$ and R^{MRS} are the spectral sampling of the detector and the spectral resolution of the actual MRS instrument, respectively, provided in [41]. The values of $T_{i'}$, $T_{l'}$, and R, along with the dimension in pixels of the measurements (I', L') are given in Table I. Finally, the simulated measurements $\boldsymbol{y}_{c,p}$ are degraded with an additive Gaussian noise with a standard deviation σ_n fixed to have a Signal-to-Noise Ratio (SNR) equals to 30 dB for each channel

$$\text{SNR} = 10 \log_{10} \left(\|\boldsymbol{y}_{c,p}\|_2^2 / N_{cp} \sigma_n^2 \right) \tag{30}$$

where $N_{c,p}$ is the size of $\boldsymbol{y}_{c,p}$. Hence, the additive Gaussian noise is non-identically distributed over the totality of the measurements $\boldsymbol{y}$.

The algorithms are implemented in Python with the Numpy library and Q-MM [2] toolbox [31] for Quadratic Majorization-Minimization, with a single CPU at 5GHz with 32 GB of memory.

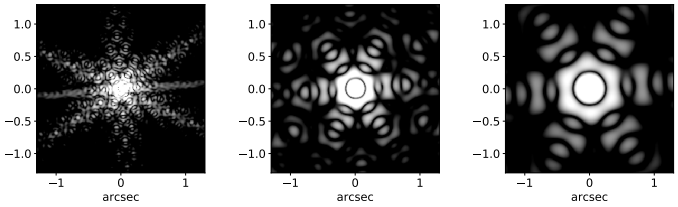

(a) $\lambda = 5\,\mu$m (b) $\lambda = 15\,\mu$m (c) $\lambda = 25\,\mu$m

Fig. 2. PSF at different wavelengths of JWST/MIRI (logarithmic scale) simulated with the WebbPSF package [27].

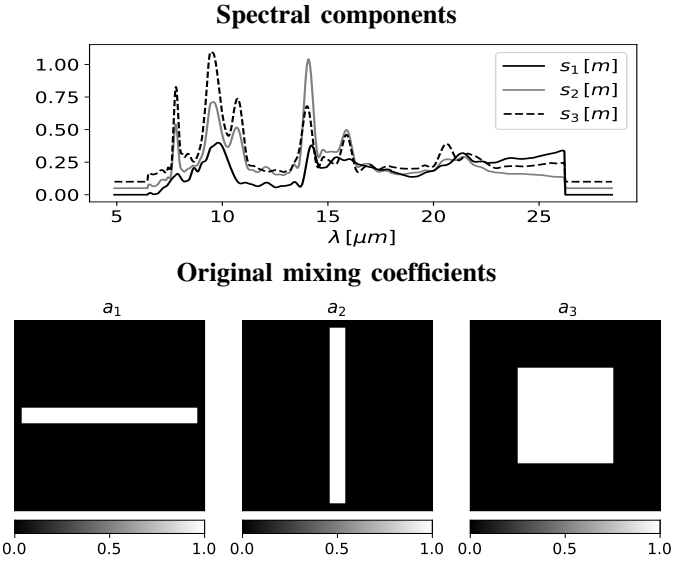

Fig. 3. Obj_1: Spectral components [top], mixing coefficients [bottom].

B. Estimation results for $\hat{\boldsymbol{a}}_m$

The estimation of the mixing coefficients $\hat{\boldsymbol{a}}_m$ depends on the overall blurred, sampled, and noisy measurements $\boldsymbol{y}$. We used the same model for the simulation and the inversion of the measurements to reconstruct the mixing coefficients for Obj_1, shown in Fig. 5 [top]. In contrast, we considered the following errors in the model to reconstruct the mixing coefficients for Obj_2 shown in Fig. 5 [bottom]: (1) the wavelength-dependent spatial PSF is spectrally shifted with an offset of $+0.25\,\mu$m (the PSF used for the reconstruction are therefore wider than the PSF used for the simulation), (2) the response of the gratings (see Eq. 4 and Fig. 1) is approximated by a Gaussian PSF, and (3) the Gaussian noise is non-identically distributed during the simulation process whereas it is identically distributed during the inversion. The red frames in Fig. 5 represent the largest observed FOV, corresponding to the *Channel 4* (see Tab. I). We are interested in reconstructing $\hat{\boldsymbol{a}}_m$ inside this FOV even if for the other channels (or wavelengths), no measurements have been made. We test our reconstruction algorithm

[2] https://github.com/forieux/qmm/

Ch.	Spectral range (μm)	FOV (pixels)	Slit width (arcsec)	Slit number	$T_{i'}$ (arcsec)	$T_{l'}$ (μm)	I' pixels	L' pixels	R
1	4.9 – 7.7	34×42	$2 \times T_j$	21	$2 \times T_i$	$4\,10^{-3}$	17	750	867
2	7.4 – 11.7	42×51	$3 \times T_j$	17	$2 \times T_i$	$6\,10^{-3}$	21	750	760
3	11.5 – 18.1	57×64	$4 \times T_j$	16	$3 \times T_i$	$9\,10^{-3}$	19	750	596
4	17.7 – 28.5	72×72	$5 \times T_j$	12	$3 \times T_i$	$1.6\,10^{-2}$	24	750	410

TABLE I
CHARACTERISTICS SPECIFIC TO THE FOUR SPECTRAL CHANNELS OF THE IFS INSTRUMENT CONSIDERED IN THIS WORK.

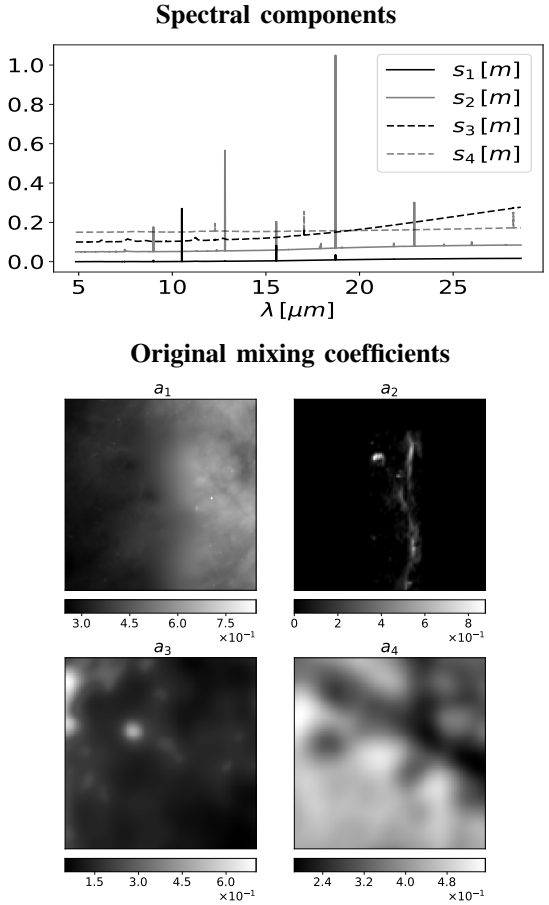

Fig. 4. Obj_2: Spectral components [top], mixing coefficients [bottom].

with a sufficient number of iterations (see Table II) to ensure convergence towards the solution $\hat{\boldsymbol{a}}_m$. The reconstruction of $\boldsymbol{a}_m$ for Obj_2 is computationally more expensive than that for Obj_1, since Obj_2 has one more spectral component.

Our proposed algorithm is based on minimizing the regularized objective function in Eq. (18) with a convex regularization function ϕ for edge-preserving. We particularly focus on the Huber potential function [23] with

$$\phi(\delta, T) = \begin{cases} \delta^2, & \text{if } |\delta| \leq T. \\ 2T|\delta| - T^2 & \text{otherwise, } T \in \mathbb{R}^+. \end{cases} \tag{31}$$

The Huber function is continuously differentiable with a quadratic form below a fixed threshold T to promote smoothness to the solution and a linear form above T to preserve the high gradient values. Consequently, two regularization parameters μ and T must be tuned to ensure the best reconstruction. Their values are reported in Table II. In practice, we have minimized the normalized least square error between the original $\boldsymbol{a}_m$ mixing coefficient and the estimated ones $\hat{\boldsymbol{a}}_m$ for both objects with

$$\text{Error}(\mu, T) = \|\boldsymbol{a}_m - \hat{\boldsymbol{a}}_m(\mu, T)\|_2 / \|\boldsymbol{a}_m\|_2. \tag{32}$$

The spatial distribution differs between $\boldsymbol{a}_m$ for Obj_2, particularly between $\boldsymbol{a}_{m=2}$ which contains sharp edges and $\boldsymbol{a}_{m\neq 2}$ which are smoother. Therefore, we have used one set of parameters (μ, T) for $m = 2$, and another one for $m \neq 2$ (see Table II).

The comparison between figures 3-4 and figure 5 shows that the reconstructed mixing coefficients $\hat{\boldsymbol{a}}_m$ for both objects are unmixed and deconvoluted while preventing noise amplification without excessive penalization of sharp edges. The normalized least square errors are as small as $0.01\,\%$ and $0.98\,\%$, for Obj_1 and Obj_2, respectively.

	Iterations	Runtime [s] per iteration	μ	T
Obj_1	455	7.8	18	0.025
Obj_2	633	10.6	0.005 ($m \neq 2$) 0.0005 ($m = 2$)	1.5 ($m \neq 2$) 0.001 ($m = 2$)

TABLE II
ITERATION NUMBERS AND HYPERPARAMETER VALUES Obj_1 AND Obj_2.

C. Hyperspectral Reconstruction

This section compares the original and the reconstructed 3D images with the proposed and state-of-the-art algorithms. The reconstructed HS images are obtained from the estimated mixing coefficients $\hat{\boldsymbol{a}}_m$ using Eq. (8). In addition to the l_2 reconstruction, the proposed results are compared to the "Shift and Add" algorithm (*S&A*) Eq. (27) followed by a TV deconvolution using Eq. (28).

We first showcase in Fig. 6 the spectral distribution at the center of the FOV of the original and the reconstructed images computed with the *S&A* and the proposed algorithms. Qualitatively the spectral distribution of the reconstructed image with the proposed algorithm matches the original spectral distribution over the whole measured range. On the other hand, the *S&A* algorithm fails to fully reconstruct the spectral distribution, particularly the spectral lines in Obj_2, which appears broader and less intense than the original ones. Such results are expected since the *S&A* algorithm does not consider the spectral blurring initially introduced by the wavelength dispersion system.

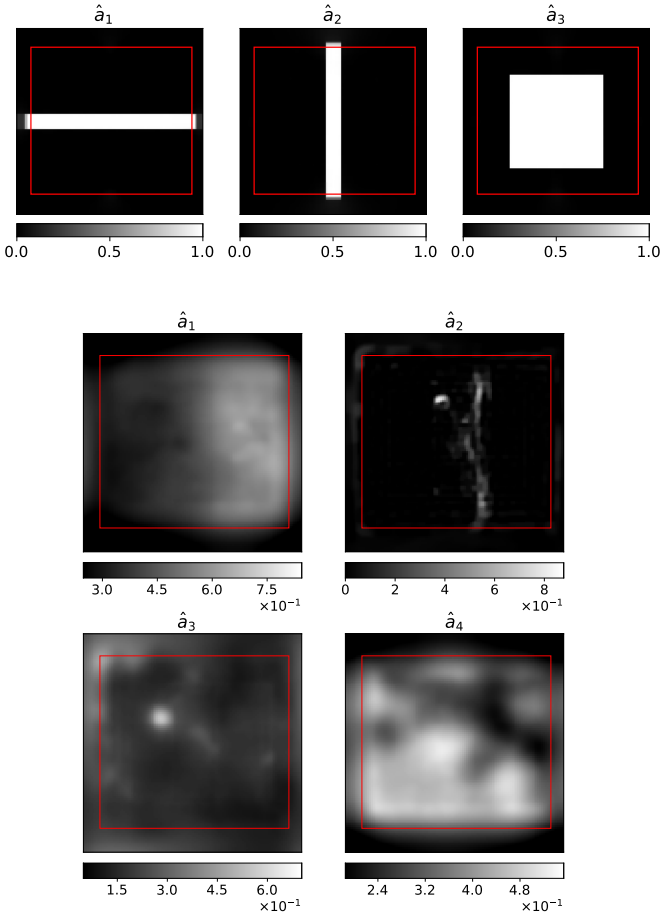

Fig. 5. Estimated mixing coefficients $\hat{\boldsymbol{a}}_m$ for Obj_1 [top], Obj_2 [bottom].

Fig. 9 illustrates the spatial distribution of the reconstructed 3D image for Obj_1 for three monochromatic images at $\lambda = 6.5$, 14 and 21 μm, respectively, belonging to channels 1, 3, and 4. The loss of spatial information caused by the detector integration is compensated in the multi-frame SR reconstruction using the *S&A* algorithm. However, since this method does not consider spectral variations of the PSF, the reconstructed images are blurred, especially at long wavelengths. We proceed by applying a TV deconvolution for each monochromatic image. This added step allows better preservation of sharp edges and smaller errors but fails to restore spatial details at a small scale since the regularization is applied separately for each monochromatic image and does not account for the correlations between spectral bands. On the other hand, the proposed algorithm shows a good performance with smaller error values for all monochromatic images. The improvement of spatial resolution is striking, and the spatial dynamic range appears fully reconstructed. Moreover, the edges in the image are well preserved, whereas the l_2 approach introduces smoothing and ringing artifacts.

Fig. 10 shows the spatial distribution of the reconstructed 3D image for Obj_2, for three monochromatic images at $\lambda = 6.5$ μm which corresponds to continuum emission, and at $\lambda = 17$ and 18.7 μm which corresponds to two different spectral lines. As mentioned earlier, the reconstructed spectral lines with the *S&A* algorithm are spectrally broadened because the spectral response is not considered. Hence, for a fair comparison between the algorithms, we have spectrally integrated the reconstructed HS image with the *S&A* algorithm over the broad reconstructed spectral line, then we proceed with the TV deconvolution for the integrated images. In all cases, our proposed algorithm shows the best qualitative reconstructions with the lowest errors for all monochromatic images. The l_2 approach gives good results with comparable errors for the smooth images but fails to preserve the sharp edges, particularly at $\lambda = 18.7$ μm as illustrated in Fig. 7. Analogously to Obj_1, the *S&A* and TV algorithms fail to fully reconstruct small-scale spatial details.

	No model errors	Model errors
PSNR	65	40
SSIM	0.99	0.99
SAM	4×10^{-4}	4×10^{-3}

TABLE III
THE PSNR, SSIM AND SAM FOR THE RECONSTRUCTED Obj_1 USING THE PROPOSED ALGORITHM, WITH AND WITHOUT ERRORS IN THE MODEL

Finally, we compare the proposed algorithm to the HS reconstruction algorithm proposed in [37]. The latter directly estimates the full 3D input from the measurements by performing a joint spatial and spectral reconstruction with a ℓ_2–ℓ_1 regularization on spatial and spectral difference (like vector-TV) and hyperparameter set to optimize the recontruction error. We validate the reconstruction on a third image Obj_3[3] that has more complex backgrounds such as small-scale spatial features and discontinuities. Fig. 11 illustrates the spatial distribution of the reconstructed 3D image for Obj_3 at $\lambda = 14\,\mu$m.

The proposed algorithm restores the spatial dynamic with an error of 2.48% while *S&A* has an error of 7.06% and [37] with vector-TV prior has an error of 3.9%. Moreover, the proposed LMM algorithm requires only the reconstructions of $\hat{\boldsymbol{a}}_m$. In contrast, the algorithm in [37] has to estimate the full HSI $\boldsymbol{x}$, yielding more errors especially at long wavelengths since the blurring is more critical. More important, the spatial hyperparameters may not be adapted at every wavelength, like for the Obj_2 case, and the introduction of additional hyperparameters makes the tunning very difficult.

D. Quality Metrics

To better evaluate the spatial and spectral performances of the reconstruction algorithms, we use three quantitative measurements:

1) the Spectral Angular Mapper (SAM) [47] measuring the spectral distortion, in radians, of the m^{th} pixel

$$\text{SAM}(m) = \arccos\left(\frac{< \boldsymbol{x}_m, \hat{\boldsymbol{x}}_m >}{\|\boldsymbol{x}_m\|_2 \|\hat{\boldsymbol{x}}_i\|_m}\right). \qquad (33)$$

where $\boldsymbol{x}_m$ and $\hat{\boldsymbol{x}}_m$ are the spectral vector of the m^{th} spatial location ($m \in [0, \ldots, I] \times [0, \ldots, J]$) of the original and reconstructed 3D images, respectively. The

[3]available here http://lesun.weebly.com/hyperspectral-data-set.html

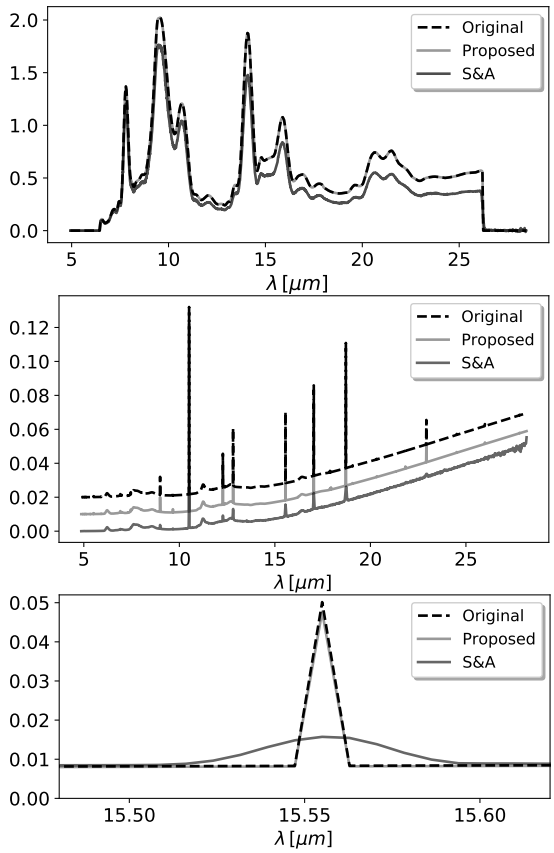

Fig. 6. Spectral distribution of the reconstructed HS image with the proposed and *S&A* algorithms, at the central spatial position (60,60) for Obj_1 [top], Obj_2 [middle: note that the three spectral distributions are shifted for clarity], zoom on a spectral line for Obj_2 [bottom].

Fig. 7. Zoom on sharp edges for Obj_2 at 18.7μm: Original [left], proposed [center], l_2 approach [right].

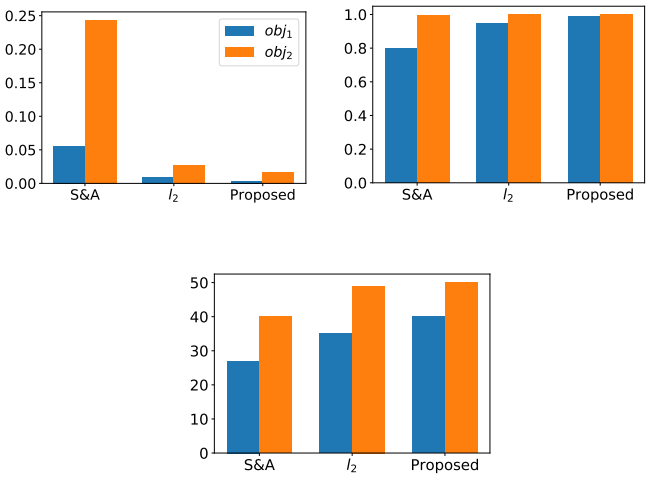

Fig. 8. Quality metrics for Obj_1 (blue) and Obj_2 (orange): Global SAM [top left], global SSIM [top right], global PSNR [bottom]

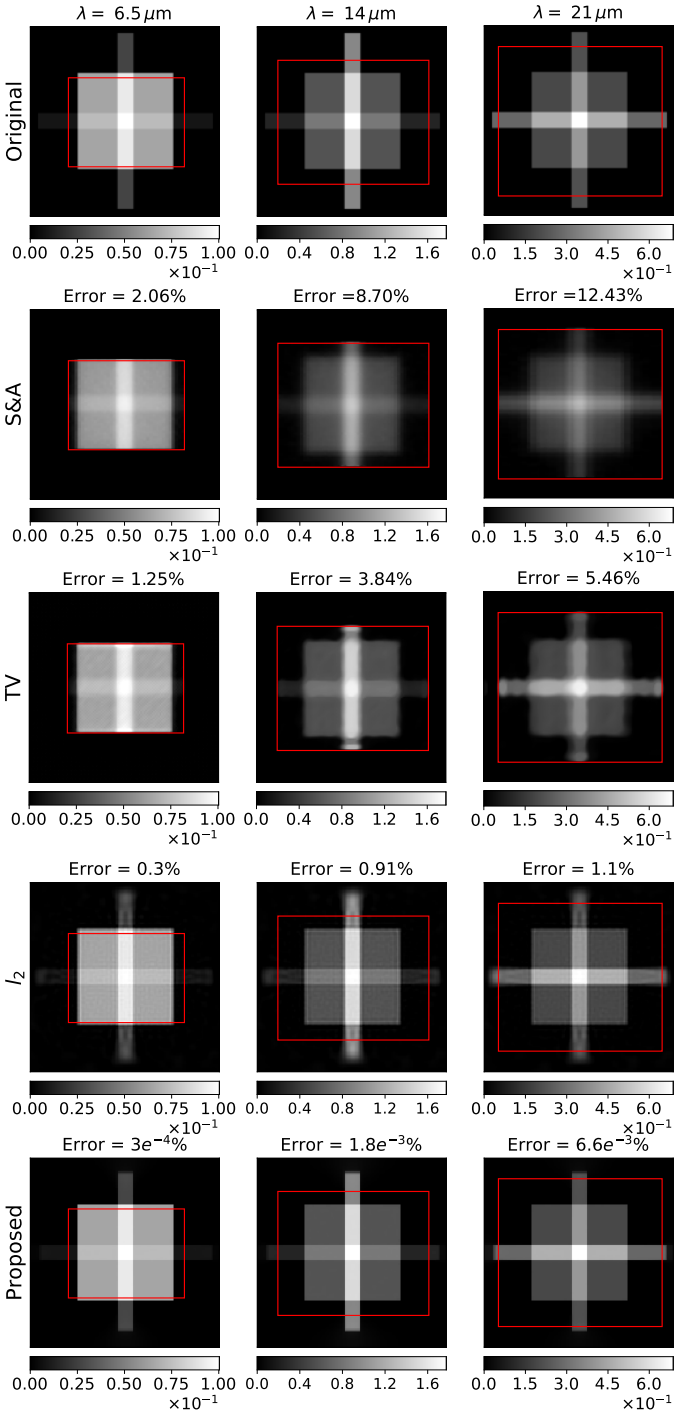

Fig. 9. Spatial reconstruction for Obj_1 : Original images at 6.5, 14, and 21 μm [1st row], *S&A* [2nd row], TV restoration [3rd row], l_2 approach [4th row], proposed [5th row].

further the SAM value is from 0, the greater the spectral distortion.

2) the peak signal-to-noise ratio (PSNR)

$$\mathrm{PSNR}(l) = 10\log_{10}\left(\frac{\max(\boldsymbol{x})^l}{\|\boldsymbol{x}^l - \hat{\boldsymbol{x}}^l\|^2}\right). \qquad (34)$$

$\mathrm{PSNR}(l)$ denotes the PSNR of the spatial image at the l^{th} spectral band of $\boldsymbol{x}$ and $\hat{\boldsymbol{x}}$.

3) the Structural Similarity Index (SSIM) [48], computed

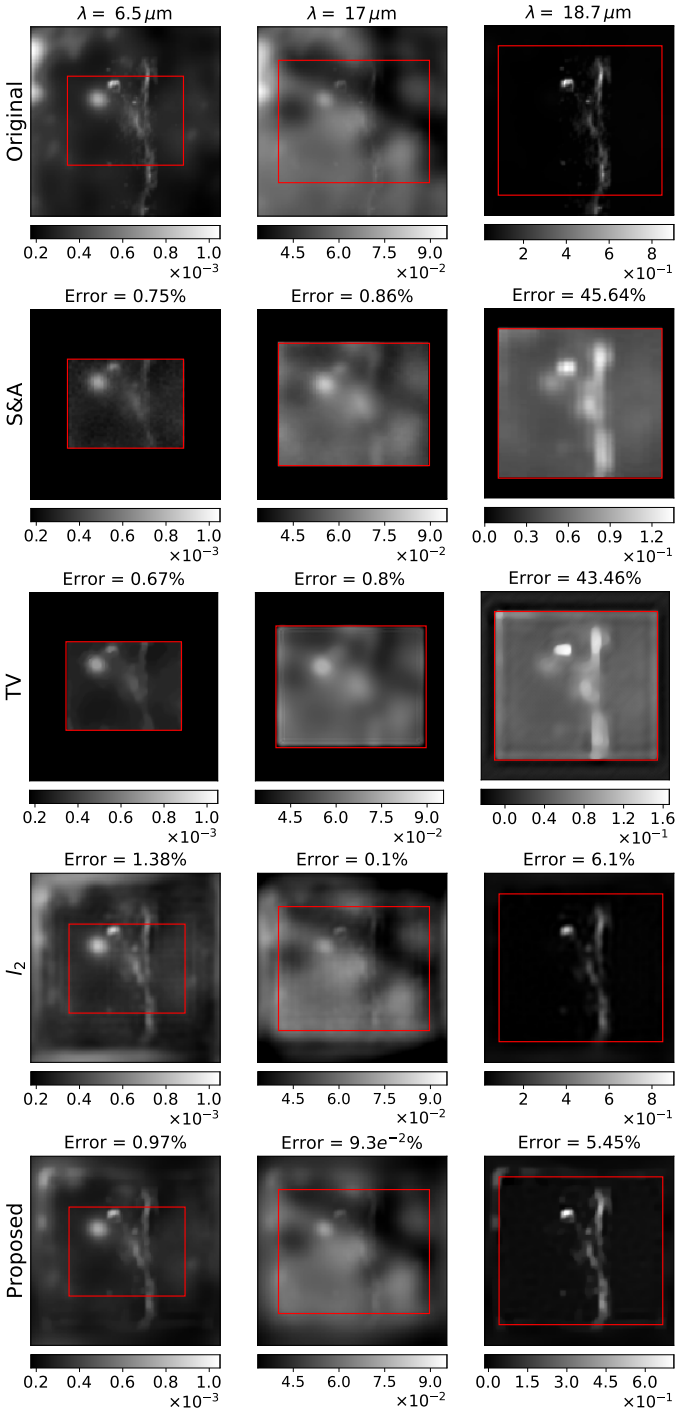

Fig. 10. Spatial reconstruction for Obj_2 : Original images at 6.5, 17, and 18.7 μm [1st row], *S&A* [2nd row], TV [3rd row], l_2 approach [4th row], proposed [5th row].

for each l^{th} spectral band, whose value varies between 0 and 1. The higher the value, the better the similarity.

The global SAM is computed by averaging the whole image, while the global PSNR and SSIM are computed by averaging all spectral bands.

Table III compares the proposed reconstruction of Obj_1 with and without model errors in terms of average SAM, SSIM, and PSNR. We illustrate in Fig. 8 the average SAM, SSIM, and PSNR for Obj_1 and Obj_2 while considering the

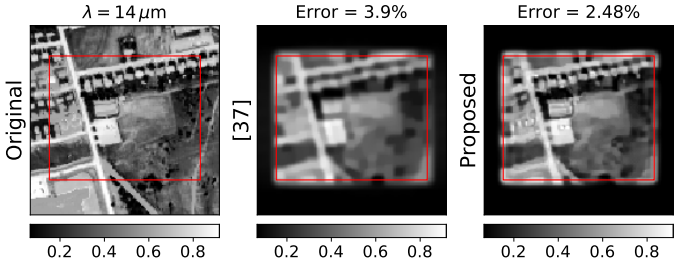

Fig. 11. Spatial reconstruction for Obj_3: Original image [left], spatial spectral reconstruction with [37] [center], proposed [right].

errors in the model during the reconstruction process. The proposed algorithm shows the best spectral reconstruction with the lowest distortion for both objects. The spectral distortion is very high for the *S&A* algorithm applied to Obj_2, due to the presence of sharp spectral lines which are hardly recovered by this algorithm. Moreover, our algorithm shows the best similarity index, especially for Obj_1. Overall, the proposed algorithm shows the best spatio-spectral reconstruction for both scenes, with the highest average PSNR values.

V. Conclusion

We present in this work a new model for hyperspectral data fusion based on low-rank approximation and a new efficient Super-Resolution algorithm for hyperspectral reconstruction based on a Quadratic Majorization-Minimization optimization algorithm.

The first contribution is to develop an explicit forward model based on IFS instruments. This model takes as input a high spatio-spectral resolution image, approximated on a low-rank subspace, and acquires a set of 2D measurements projected onto different detectors with different characteristics. The complex forward model takes into account (1) different observations of the same scene with sub-pixel shifts, (2) wavelength-dependent spatial and spectral PSFs, (3) different spectral channels and IFUs, observing the input with different spectral ranges and different numbers of slits of different sizes, and finally (4) heterogeneous spatio-spectral samplings.

The second contribution is a fusion of the multi-frame blurred and sampled 2D measurements, acquired from different spectral channels, in order to restore the single HSI observed input. The algorithm is based on the regularized least square approach with convex edge-preserving regularization, and solved via the iterative Majorize-Minimize Memory Gradient (3MG) [24] optimization algorithm, with freely provided code [4].

Our method allows joint spectral unmixing with spatial and spectral enhancements. The known spectral components serve as a spectral regularization to our approach and prevent spectral distortion, whereas the multi-frame observations and the enforced spatial regularization allow restoring the original spatial distribution without excessive penalization of high gradient values.

Our work is validated with relative errors below 1% over the whole reconstructed HS images for an SNR = 30 dB. Our

[4] http://github.com/forieux/qmm

algorithm outperformed qualitatively and quantitatively the l_2 approach, as well as the standard *S&A* and TV deconvolution algorithms.

Several perspectives can be considered. First, non-convex regularization or data-learned prior may be envisaged for better resolution of the reconstruction. The spatial and spectral resolutions of the reconstructed 3D image can also be enhanced by performing a fusion between the IFS measurements with a high spectral but low spatial resolution, considered in this work, and multispectral measurements with a high spatial but low spectral resolution, observing the same scene. The fusion problem can be solved in the inverse problem framework [1]. In addition, the spectral components of the LMM are, in many applications, not provided *a priori* and must be extracted or learned directly from the measurements along with the mixing coefficients [49]. In a wider perspective, we would like to estimate the hyperparameters jointly with the 3D input image instead of being fixed by hand. The problem can be formulated in the Bayesian framework where the solution is deduced from *a posteriori* law for the unknown hyperparameters and the 3D input image [50].

ACKNOWLEDGMENT

We thank Jérôme Idier (LS2N – CNRS) and Saïd Moussaouï (LS2N – École Centrale de Nantes) for fruitful discussions about MM optimization, Olivier Berné (IRAP – CNRS) for Obj_1 spectra, and Claire Guilloteau (INSA Rouen) for providing the Orion bar spectra and maps (Obj_2).

REFERENCES

[1] C. Guilloteau, T. Oberlin, O. Berné, and N. Dobigeon, "Hyperspectral and multispectral image fusion under spectrally varying spatial blurs – application to high dimensional infrared astronomical imaging," *IEEE Transactions on Computational Imaging*, vol. 6, pp. 1362–1374, 2020.

[2] J. G. Dwight and T. S. Tkaczyk, "Lenslet array tunable snapshot imaging spectrometer (latis) for hyperspectral fluorescence microscopy," *Biomed. Opt. Express*, vol. 8, no. 3, pp. 1950–1964, Mar 2017. [Online]. Available: http://www.osapublishing.org/boe/abstract.cfm?URI=boe-s8-s3-s1950

[3] M. Shimoni, R. Haelterman, and C. Perneel, "Hypersectral imaging for military and security applications: Combining myriad processing and sensing techniques," *IEEE Geoscience and Remote Sensing Magazine*, vol. 7, no. 2, pp. 101–117, 2019.

[4] G. Lu and B. Fei, "Medical hyperspectral imaging: a review," *Journal of Biomedical Optics*, vol. 19, no. 1, pp. 1 – 24, 2014. [Online]. Available: https://doi.org/10.1117/1.JBO.19.1.010901

[5] S. Vives, E. Prieto, Y. Salaun, and P. Godefroy, "New technological developments in integral field spectroscopy," in *Advanced Optical and Mechanical Technologies in Telescopes and Instrumentation*, E. Atad-Ettedgui and D. Lemke, Eds., vol. 7018, International Society for Optics and Photonics. SPIE, 2008, pp. 959 – 968. [Online]. Available: https://doi.org/10.1117/12.789576

[6] J. W. Goodman, *Introduction to Fourier Optics McGraw-Hill Series in Electrical and Computer Engineering*, 1996, vol. 8, no. 5. [Online]. Available: http://stacks.iop.org/1355-s5111/8/i=5/a=014?key=crossref.ad20ea108e8f625cb0486bf680f74198

[7] J.-P. Pérez, *Optique - Fondements et applications*. Paris, France:Dunod, 2004.

[8] A. S. Fruchter and R. N. Hook, "Drizzle: A method for the linear reconstruction of undersampled images," *Publications of the Astronomical Society of the Pacific*, vol. 114, no. 792, pp. 144–152, feb 2002. [Online]. Available: https://doi.org/10.1086%2F338393

[9] R. Hook and A. Fruchter, "Dithering, sampling and image reconstruction," vol. 216, p. 521, 01 2000.

[10] Sung Cheol Park, Min Kyu Park, and Moon Gi Kang, "Super-resolution image reconstruction: a technical overview," *IEEE Signal Processing Magazine*, vol. 20, no. 3, pp. 21–36, May 2003.

[11] M. Elad and Y. Hel-Or, "A fast super-resolution reconstruction algorithm for pure translation motion and common space-invariant blur," *IEEE Transactions on Image Processing*, vol. 10, pp. 1187–1193, 01 2001.

[12] L. I. Rudin, S. Osher, and E. Fatemi, "Nonlinear total variation based noise removal algorithms," *Physica D: Nonlinear Phenomena*, vol. 60, no. 1, pp. 259–268, 1992. [Online]. Available: https://www.sciencedirect.com/science/article/pii/016727899290242F

[13] H. Shen and L. Zhang, "A map-based algorithm for destriping and inpainting of remotely sensed images," *IEEE Transactions on Geoscience and Remote Sensing*, vol. 47, no. 5, pp. 1492–1502, 2008.

[14] T. Akgun, Y. Altunbasak, and R. M. Mersereau, "Super-resolution reconstruction of hyperspectral images," *IEEE Transactions on Image Processing*, vol. 14, no. 11, pp. 1860–1875, 2005.

[15] H. Zhang, L. Zhang, and H. Shen, "A super-resolution reconstruction algorithm for hyperspectral images," *Signal Processing*, vol. 92, no. 9, pp. 2082 – 2096, 2012. [Online]. Available: http://www.sciencedirect.com/science/article/pii/S0165168412000345

[16] Y. Chang, L. Yan, X.-L. Zhao, H. Fang, Z. Zhang, and S. Zhong, "Weighted low-rank tensor recovery for hyperspectral image restoration," *IEEE transactions on cybernetics*, vol. 50, no. 11, pp. 4558–4572, 2020.

[17] H. Stark and P. Oskoui, "High-resolution image recovery from image-plane arrays, using convex projections," *J. Opt. Soc. Am. A*, vol. 6, no. 11, pp. 1715–1726, Nov 1989. [Online]. Available: http://josaa.osa.org/abstract.cfm?URI=josaa-s6-s11-s1715

[18] I. T. Jolliffe and J. Cadima, "Principal component analysis: a review and recent developments," *Philosophical Transactions of the Royal Society A: Mathematical, Physical and Engineering Sciences*, vol. 374, 2016.

[19] R. Schultz and R. Stevenson, "Extraction of high-resolution frames from video sequences," *IEEE transactions on image processing : a publication of the IEEE Signal Processing Society*, vol. 5, pp. 996–1011, 02 1996.

[20] G. Vivone, L. Alparone, J. Chanussot, M. Dalla Mura, A. Garzelli, G. Licciardi, R. Restaino, and L. Wald, "A critical comparison among pansharpening algorithms," vol. 53, 07 2014.

[21] Q. Wei, J. Bioucas-Dias, N. Dobigeon, and J. Tourneret, "Hyperspectral and multispectral image fusion based on a sparse representation," *IEEE Transactions on Geoscience and Remote Sensing*, vol. 53, no. 7, pp. 3658–3668, 2015.

[22] M. Simões, J. M. Bioucas-Dias, L. B. Almeida, and J. Chanussot, "A convex formulation for hyperspectral image superresolution via subspace-based regularization," *CoRR*, vol. abs/1411.4005, 2014. [Online]. Available: http://arxiv.org/abs/1411.4005

[23] J. Idier, "Convex half-quadratic criteria and interacting auxiliary variables for image restoration," *IEEE Transactions on Image Processing*, vol. 10, no. 7, pp. 1001–1009, July 2001.

[24] E. Chouzenoux, J. Idier, and S. Moussaoui, "A majorize–minimize strategy for subspace optimization applied to image restoration," *IEEE Transactions on Image Processing*, vol. 20, no. 6, pp. 1517–1528, 2011.

[25] A. N. Tikhonov, A. Goncharsky, V. V. Stepanov, and A. G. Yagola, *Numerical Methods for the Solution of Ill-Posed Problems*, ser. Mathematics and Its Applications. Springer Netherlands, 1995. [Online]. Available: https://www.springer.com/gp/book/9780792335832

[26] J. Adams, M. Smith, and P. Johnson, "Spectral mixture modeling: A new analysis of rock and soil types at the viking lander 1 site," *Journal of Geophysical Research*, vol. 91, pp. 8098–8112, 1986.

[27] M. D. Perrin, R. Soummer, E. M. Elliott, M. D. Lallo, and A. Sivaramakrishnan, "Simulating point spread functions for the James Webb Space Telescope with WebbPSF," in *Space Telescopes and Instrumentation 2012: Optical, Infrared, and Millimeter Wave*, M. C. Clampin, G. G. Fazio, H. A. MacEwen, and J. M. O. Jr., Eds., vol. 8442, International Society for Optics and Photonics. SPIE, 2012, pp. 1193 – 1203. [Online]. Available: https://doi.org/10.1117/12.925230

[28] B. Hunt, "A matrix theory proof of the discrete convolution theorem," *IEEE Transactions on Audio and Electroacoustics*, vol. 19, no. 4, pp. 285–288, 1971.

[29] O. K. Ersoy, *Diffraction, Fourier optics and imaging*. John Wiley & Sons, 2006, vol. 30.

[30] D. D. Lee and H. S. Seung, "Learning the parts of objects by nonnegative matrix factorization," *Nature*, vol. 401, pp. 788–791, 1999.

[31] F. Orieux and R. Abirizk, "Q-mm: The quadratic majorize-minimize python toolbox." [Online]. Available: https://github.com/forieux/qmm

[32] Y. Zhao, J. Yang, Q. Zhang, L. Song, Y. Cheng, and Q. Pan, "Hyperspectral imagery super-resolution by sparse representation and spectral regularization," *EURASIP Journal on Advances in Signal Processing*, vol. 2011, no. 1, pp. 1–10, 2011.

[33] T. Zhang, Y. Fu, L. Wang, and H. Huang, "Hyperspectral image reconstruction using deep external and internal learning," in *2019 IEEE/CVF*

International Conference on Computer Vision (ICCV), 2019, pp. 8558–8567.
[34] E. Chouzenoux and J.-C. Pesquet, "Convergence rate analysis of the majorize–minimize subspace algorithm," *IEEE Signal Processing Letters*, vol. 23, no. 9, pp. 1284–1288, 2016.
[35] D. Geman and G. Reynolds, "Constrained restoration and the recovery of discontinuities," *IEEE Transactions on Pattern Analysis and Machine Intelligence*, vol. 14, no. 3, pp. 367–383, 1992.
[36] M. Allain, J. Idier, and Y. Goussard, "On global and local convergence of half-quadratic algorithms," *IEEE Transactions on Image Processing*, vol. 15, no. 5, pp. 1130–1142, 2006.
[37] R. Abi-rizk, F. Orieux, and A. Abergel, "Non-stationary hyperspectral forward model and high-resolution," in *2020 IEEE International Conference on Image Processing (ICIP)*, 2020, pp. 2975–2979.
[38] C. Labat and J. Idier, "Doi 10.1007/s10957-007-9306-x convergence of conjugate gradient methods with a closed-form stepsize formula," *Journal of Optimization Theory and Applications*, vol. 136, pp. 43–60, 01 2008.
[39] J. Nocedal, "Conjugate gradient methods and nonlinear optimization," *Linear and nonlinear conjugate gradient-related methods*, pp. 9–23, 1996.
[40] M. Zibulevsky, "Sesop-tn: Combining sequential subspace optimization with truncated newton method," Computer Science Department, Technion, Tech. Rep., 2008.
[41] M. Wells, J. W. Pel, A. Glasse, G. Wright, G. Kroes, R. Azzollini, S. Beard, B. Brandl, A. Gallie, V. C. Geers, A. M. Glauser, P. Hastings, T. Henning, R. Jager, K. Justtanont, B. Kruizinga, F. Lahuis, D. Lee, I. Martinez Delgado, and D. Wright, "The mid-infrared instrument for the james webb space telescope, vi: The medium resolution spectrometer," *Publications of the Astronomical Society of the Pacific*, vol. 127, pp. 646–664, 07 2015.
[42] S. Farsiu, D. Robinson, M. Elad, and P. Milanfar, "Robust shift and add approach to superresolution," in *Applications of Digital Image Processing XXVI*, A. G. Tescher, Ed., vol. 5203, International Society for Optics and Photonics. SPIE, 2003, pp. 121 – 130. [Online]. Available: https://doi.org/10.1117/12.507194
[43] A. Chambolle and T. Pock, "A first-order primal-dual algorithm for convex problems with applications to imaging," *Journal of Mathematical Imaging and Vision*, vol. 40, 05 2011.
[44] J. R. Shewchuk *et al.*, "An introduction to the conjugate gradient method without the agonizing pain," 1994.
[45] O. Berné, C. Joblin, Y. Deville, J. D. Smith, M. Rapacioli, J. P. Bernard, J. Thomas, W. Reach, and A. Abergel, "Analysis of the emission of very small dust particles from Spitzer spectro-imagery data using blind signal separation methods," *Astronomy and Astrophysics - A&A*, vol. 469, pp. 575–586, July 2007, 14 pages, 11 figures, to appear in A&A. [Online]. Available: https://hal.archives-souvertes.fr/hal-s00287344
[46] C. Guilloteau, T. Oberlin, O. Berné, E. Habart, and N. Dobigeon, "Simulated jwst data sets for multispectral and hyperspectral image fusion," *The Astronomical Journal*, vol. 160, no. 1, p. 28, Jun 2020. [Online]. Available: http://dx.doi.org/10.3847/1538-s3881/ab9301
[47] Chein-I Chang, "An information-theoretic approach to spectral variability, similarity, and discrimination for hyperspectral image analysis," *IEEE Transactions on Information Theory*, vol. 46, no. 5, pp. 1927–1932, 2000.
[48] Zhou Wang, A. C. Bovik, H. R. Sheikh, and E. P. Simoncelli, "Image quality assessment: from error visibility to structural similarity," *IEEE Transactions on Image Processing*, vol. 13, no. 4, pp. 600–612, 2004.
[49] S. Henrot, C. Soussen, M. Dossot, and D. Brie, "Does deblurring improve geometrical hyperspectral unmixing?" *IEEE Transactions on Image Processing*, vol. 23, no. 3, pp. 1169–1180, 2014.
[50] N. Dobigeon, S. Moussaoui, M. Coulon, J.-Y. Tourneret, and A. O. Hero, "Joint bayesian endmember extraction and linear unmixing for hyperspectral imagery," *IEEE Transactions on Signal Processing*, vol. 57, no. 11, pp. 4355–4368, 2009.

Ralph Abi Rizk received his Ph.D degree in image and signal processing from Laboratoire signaux et systèmes (Université Paris-Saclay, CNRS, CentraleSupélec), France in 2021. He is currently a post-doctoral researcher at Laboratoire des Sciences du Numérique de Nantes, Centrale Nantes, France. His research interests include inverse problem approaches, hyperspectral image reconstruction, and ultrasound image processing for non destructive testing (NDT).

François Orieux is Assistant Professor at the Université Paris-Saclay in the Laboratoire des Signaux et Systèmes, Groupe Problèmes Inverses (Université Paris-Saclay, CNRS, CentraleSupélec), France. He is also an associate researcher with the Institut d'Astrophysique Spatiale (Univ. Paris- Saclay, CNRS). He received his Ph.D. degree in signal processing at Université Paris-Sud, Orsay, France. His research focuses on Bayesian methodological approaches for ill-posed inverse problem resolution with examples of applications in astrophysics or biological microscopy.

Alain Abergel is professor of Physics and Astrophysics at the Paris-Saclay University. He is an astrophysicist of the interstellar medium at the Institut d'Astrophysique Spatiale (Paris-Saclay University, CNRS), and is involved in the scientific exploitation of several space missions for astrophysics (ISO, Spitzer, Herschel, Planck, JWST, ...).